ELSEVIER

Contents lists available at ScienceDirect

Thin-Walled Structures

journal homepage: www.elsevier.com/locate/tws





Numerical modelling of solid slab push-out tests with stainless steel welded stud shear connectors

R. Presswood ^{a, b, *}, M. Shaheen ^b, S. Afshan ^a, F. Meza ^c, N. Baddoo ^c

- ^a Faculty of Engineering and Physical Sciences, University of Southampton, United Kingdom
- b School of Architecture, Building and Civil Engineering, Loughborough University, United Kingdom
- ^c The Steel Construction Institute, United Kingdom

ARTICLE INFO

Keywords: Composite beam Numerical modelling Push-out tests Shear connector Stainless steel

ABSTRACT

Push-out tests on composite steel–concrete beams are a standardised method for assessing the load-slip capacity of shear connectors, such as welded headed studs. Experimental push-out tests can be costly and time-consuming, so finite element (FE) numerical analyses provide an alternative for producing data on shear stud performance via parametric analyses, provided the numerical model has been accurately validated. Stainless steel has recently gained attention for use in composite construction due to its excellent durability, as well as ductility and strain hardening properties. Very few experimental push-out tests have been conducted on stainless steel shear studs in solid slabs, partly due to the high costs of stainless steel materials. Following a review of common push-out modelling approaches in the literature, this paper presents a comprehensive framework for FE modelling of stainless steel push-out tests, including ductile damage for the welded studs, which can be applied to different stud grades, geometries and arrangements. The modelling approach is demonstrated to accurately capture elastic, plastic and post-peak load-slip response, as well as failure mode, from three distinct test programs on stainless steel and carbon steel welded shear studs. A parametric study is carried out to investigate the effects of stud aspect ratio h/d on the capacity and ductility of austenitic EN 1.4301 stainless steel studs, and the results are compared to the recommended h/d limit in Eurocode 4.

1. Introduction

Push-out tests on composite steel-concrete specimens are a standardised method for experimentally measuring the load and slip capacities of shear connectors in composite beams. The test methodology is detailed in several design standards, including Annex B of Eurocode 4 [1]. While push-out tests do not wholly simulate the behaviour of studs in composite beams, mainly due to the absence of bending stresses within the concrete slab, full-scale composite beam tests are costly and time consuming. Furthermore, it is difficult to quantify the shear force transferred by individual studs within a composite beam, therefore push-out tests are preferred as a simpler method which provide conservative strength and slip capacity measurements for studs [2,3]. Welded headed studs are the most common type of shear connector used in composite construction [4-10]. However, in recent years, demountable bolted shear studs have gained interest due to their sustainable advantages, as they enable composite slabs to be disassembled and reused at the end of a structure's life cycle. As a result, push-out tests on demountable specimens using bolted shear studs have been carried out to investigate their performance [11-13]. Another recent development in composite construction is the use of stainless steel beams and shear studs, due to their excellent corrosion resistance owing to the addition of chromium to the alloy. Using stainless steel for the girder in composite bridges, especially bridges located in high chloride environments, can significantly reduce life cycle costs due to reduced maintenance costs, as well as indirect user costs due to fewer journey disruptions. Carbon emissions can also be reduced, both directly (e.g., eliminating corrosion resistant paint) and indirectly (e.g., fewer traffic disruptions, greenhouse gas emissions due to standing traffic) [14,15].

To enable their application in construction, new design codes are being developed to address the specific requirements of stainless steel-concrete composite beams. In this context, new test data have been reported, including studies by Zhou et al. [9] on stainless steel composite beams and shear studs at the University of Sydney, and by Presswood et al. [16] on stainless steel shear studs at the University of Southampton. Conducting push-out tests is time-consuming and expensive, particularly with the higher material costs of stainless steels. Therefore, finite element (FE) modelling provides a more convenient alternative for generating extensive structural performance data through

E-mail address: r.s.presswood@soton.ac.uk (R. Presswood).

^{*} Corresponding author.

parametric analyses to investigate the effect that different parameters may have on the behaviour and capacity of stainless steel shear studs in composite beams. The data generated can be used to assess the reliability of design equations.

Numerical models of push-out tests have been developed in FE modelling software ABAQUS [17] and used in the literature to conduct several parametric studies on carbon steel welded studs in solid concrete slabs. Common parameters investigated include concrete strength, stud diameter and stud height-to-diameter ratio. Pathirana et al. [4], Li et al. [8] and Lam and Ellobody [10] investigated the impact of concrete slab compressive strength on the push-out behaviour while Xu et al. [5] compared the response of studs embedded in lightweight and normal-weight concrete. Pathirana et al. [4], Li et al. [8] and Pavlovic et al. [11] studied the effect of stud height-to-diameter ratio, while Kruszewski et al. [6] investigated the importance of stud diameter relative to the beam web thickness, as well as the influence of eccentric loading in push-out experiments. Kruszewski et al. [6] modelled specimens with ultra-high performance concrete (UHPC), as did Li et al. [8], who also examined the effect of concrete cover thickness and stud arrangement. In addition to the research on solid slabs with welded shear studs, Katwal et al. [7] modelled push-out tests with profiled steel sheeting, and Pathirana et al. [4], Pavlovic et al. [11], Tzouka et al. [12] and He at al. [13] modelled push-out specimens with bolted shear studs. Numerical analyses of push-out specimens containing welded stainless steel shear studs and stainless steel-concrete composite beams have only been reported by Zhou et al. [9], who also developed push-out models with bolted shear studs, where the use of stainless steel in demountable construction was examined.

The existing literature on numerical modelling studies of steelconcrete push-out specimens lacks consensus on the most suitable modelling methodology and assumptions. There are, for example, contradicting approaches regarding boundary conditions and contact definitions. Additionally, there are differences in the focus of the model validation requirements, with many studies prioritising the ultimate load or the load-slip response up to the ultimate load, often neglecting considerations of the post-ultimate load characteristics and the associated material damage modelling. Therefore, a robust validated approach for push-out modelling incorporating post-peak softening behaviour is required to enable reliable parametric studies to be conducted. To address this, this paper presents a comprehensive review and assessment of various push-out modelling approaches employed in the literature, highlighting contradictions between, and sensitivity to, modelling assumptions and parameters. Following this, a detailed description of the proposed modelling framework is presented, which simulates the response of push-out specimens using both carbon and stainless steel welded headed shear studs. In developing the model, the focus was on accurately capturing the full load-slip response, including elastic, plastic, and softening stages as well as the failure mode, which required the calibration of ductile damage parameters; two methods for calibrating Bao-Wierzbicki damage parameters [18,19] are described and compared. The validity of the proposed modelling framework incorporating ductile damage is demonstrated through comparisons with push-out results, including new test data from stainless steel pushout tests conducted by the authors [16], and those reported in the literature [4,9]. The proposed modelling approach can be applied to different stud material grades, diameters, heights and arrangements, provided the model ductile damage parameters are carefully calibrated against test data.

The validated model is used to investigate the transfer of loads within the push-out tests, focusing on friction and bearing forces at the steel–concrete and stud-concrete interfaces. Finally, a parametric study is carried out to assess the effects of stud aspect ratio h/d on the capacity and ductility of austenitic EN 1.4301 stainless steel welded shear studs. The results are compared to the h/d limit for carbon steel shear studs given by Eurocode 4.

2. Review of existing finite element modelling approaches

The modelling approaches employed in previous push-out studies were thoroughly examined, and the ten most commonly used approaches are summarised in Table 1. These approaches are discussed in detail in the following sections, highlighting their key features, assumptions and limitations.

2.1. Boundary conditions at support

Steel-concrete push-out models involve various elements that require complex contact formulations and fine mesh topologies, which can significantly increase computational time, particularly when accounting for plastic and softening behaviours. In order to reduce the computational time, previous researchers typically modelled either a quarter or half of the push-out specimen, depending on the applied loading, boundary conditions and the arrangements of the shear studs, through definition of appropriate quarter or half symmetry boundary conditions as reported in Table 1. Different boundary conditions at the concrete slab supports, both in terms of the restrained direction and the simulation approach, were also adopted as presented in Table 1. Some studies applied constraints to a reference point (RP) tied to the concrete slab base surface (Fig. 1a), while others applied the constraints directly to the slab base surface (Fig. 1b). These constraints can be classified as fixed (no displacements or rotations permitted), pinned (some rotations permitted) or roller (displacement normal to the slab i.e., U_{τ} permitted). In test setups, it is common for the concrete slab base to bear on a strong floor or plate, sometimes with a thin layer of grout or sand to ensure even contact, without the application of any active restraining device. Thus, a compression-only support condition should be simulated at the base of the slab, in which only displacements in the direction of the load (negative U_v as per Fig. 1) are prevented. This can be achieved by defining an analytical rigid surface beneath the slab and specifying surface-to-surface contact interaction with friction between the base surface of the slab and the analytical rigid surface. However, as shown in Table 1, some studies restrain both displacement and rotation at the slab base, which may deviate from the real boundary conditions used in the tests and can introduce erroneous tension in the base of the slab. For the applied load, few details of the loading constraints and boundary conditions are provided in the literature.

2.2. Model discretisation

Solid elements, such as C3D8R linear brick elements with reduced integration available in ABAQUS element library, have commonly been used to discretise the stud, beam and slab components. In some modelling studies, with higher strength concrete and/or smaller stud diameters, the steel reinforcement bars were not explicitly modelled, as it was shown both numerically [11] and experimentally [20,21] that reinforcement had little influence on the shear resistance of welded studs when stud shear failure dominated. However, the amount of reinforcement does affect the load capacity and crack propagation in tests where concrete failure dominates i.e., with larger diameters and/or weaker strength concrete [11,20]. In cases where reinforcement was modelled, the T3D2 truss elements were commonly employed. A range of mesh sizes was used for each component. A fine mesh of 2-4 mm was typically applied to the stud, while non-uniform mesh topologies were employed for the beam and the slab, involving a fine mesh (2-5 mm) near the stud, where high stress concentrations occur, and a coarser mesh (15 mm) in areas away from the stud location. In the models developed by Lam and Ellobody [10], a coarse mesh size of 20-60 mm was adopted for all components, but since no material damage was considered, as the concrete and steel materials were modelled as elastic-plastic, a coarse mesh was deemed sufficient.

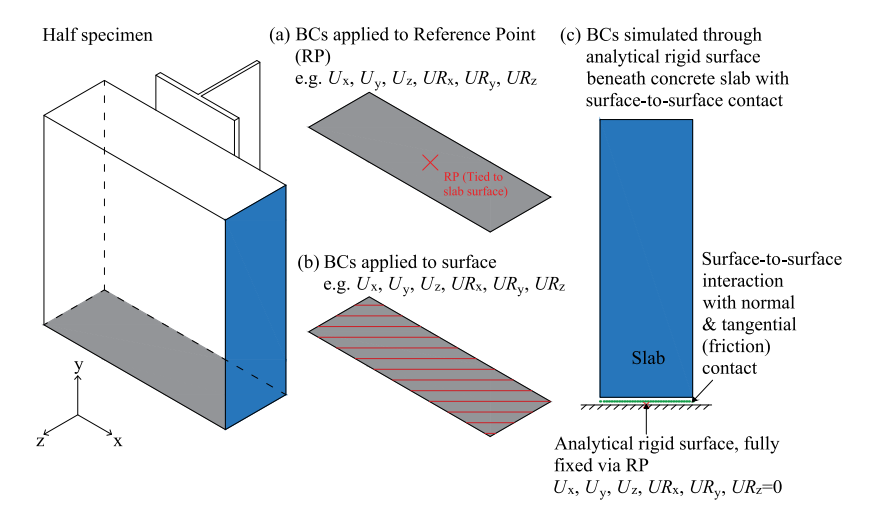


Fig. 1. Different approaches to modelling concrete slab boundary conditions in push-out tests.

Summary of push-out test modelling approaches in the literature.

Ref	Stud type	Analysis solver Mesh element type					Friction coefficient μ_{fr}	Simulation of weld	Boundary conditions	Stud damag
			Stud	Slab	Beam	Rebar	-			
1]	Welded &	Not reported	Solid (C3D8R)	Solid (C3D8R)	Solid	Truss	0.4	Studs "tie" constraint to	Half model symmetry	No
	bolted				(C3D8R)	(T3D2)		beam	Fixed support (RP/Surface not specified): $U_X = U_V = U_Z = UR_X = UR_V = UR_Z = 0$	
5]	Welded	Not reported	Solid (C3D8R)) Solid (C3D8R)	Solid (C3D8R)	Truss (T3D2)	Exponential decay friction model	Studs (with weld collars) & beam merged	Quarter model symmetry Support not reported	Lemaitre
5]	Welded	Dynamic Explicit	Solid (C3D8R)	Solid (C3D8R)	Solid (C3D8R)	None	0.4 Damping coefficient 0.8	Studs (with weld collars) & beam merged	Quarter model symmetry Roller support (RP): $U_x = U_y = 0$	SMCS
7]	Welded; profiled sheeting	Dynamic Implicit (Standard)	Solid (C3D8R)) Solid (C3D8R)	Solid (C3D8R)	Truss (T3D2)	0.25 for slab to sheeting, 0.01 for slab to studs	Studs & beam merged	Quarter model symmetry Fixed support (RP/Surface not specified): $U_X = U_Y = U_Z = UR_X = UR_Y = UR_Z = 0$ Half model symmetry Fixed support (above) and roller support:	Implicitly modelled in material plasticity
3]	Welded	General Static (Standard)	Solid (C3D8R)) Solid (C3D8R)	Solid (C3D8R)	None	0.4	Studs (with weld collars) & beam merged	Fixed support (author) and other support. $U_X = U_y = UR_X = UR_y = UR_z = 0$ Quarter model symmetry Pinned support (surface): $U_X = U_y = U_z = 0$	SMCS
)]	Welded & bolted	Dynamic Explicit	Solid (C3D8R)) Solid (C3D8R)	Solid (C3D8R)	Truss (T3D2)	0.4	Studs (with weld collars) "tie" constraint to beam	Half model symmetry Fixed support (RP): $U_X = U_y = U_z = UR_X = UR_y = UR_z = 0$ Roller support (RP):	SMCS
0]	Welded	RIKS (Standard)	Solid (C3D15, C3D20)	Solid (C3D8, C3D15)	Not reported	None		Not reported	$U_X = U_y = UR_X = UR_y = UR_Z = 0$ Quarter model symmetry Pinned support (surface):	No
1]	Bolted	Dynamic Explicit	Solid (C3D4)	Solid (C3D4)	Solid (C3D4)	Not reported	10.14	N/A	$U_y = 0$ Quarter model symmetry Fixed support (RP):	SMCS
[2]	Bolted	Dynamic Explicit	Solid (C3D8R)) Solid (C3D8R)	Solid (C3D8R)	Truss (T3D2)	0.45	N/A	$U_X = U_y = UR_X = UR_y = UR_Z = 0$ Quarter model symmetry Fixed support (surface):	SMCS
3]	Bolted	Dynamic Explicit	Solid (C3D8R)) Solid (C3D8R)	Solid (C3D8R)	Truss (T3D2)	0.4	N/A	$U_X = U_y = U_z = UR_X = UR_y = UR_z = 0$ Half model symmetry Horizontal test; fixed support (surface): $U_X = U_y = U_z = UR_X = UR_y = UR_z = 0$	No

SMCS = Stress Modified Critical Strain

C3D4 = 4-node linear tetrahedral element: C3D8R = 8-node linear brick element, with reduced integration:

C3D15 = 15-node quadratic triangular prism element; C3D20 = 20-node quadratic brick element; T3D2 = 3D Linear truss elements

2.3. Contact formulation

The most common method of contact formulation between the steel parts (beam and studs) and the concrete slab is surface-to-surface contact. The hard contact relationship defines the normal behaviour, where the secondary surface (in this case, the beam flange or the stud) is unable to penetrate the main surface (in this case, the slab) and there is no transfer of tensile stresses. Tangential contact is defined using penalty friction, typically with a representative friction coefficient μ_{fr} between steel and concrete as reported in Table 1. Kruszewski et al. [6] added a damping coefficient of 0.8 to promote stability during damage initiation of the stud and concrete. A more advanced friction approach, using an exponential friction decay model, was reported in only one study by Xu et al. [5]. When modelling welded studs, two approaches are commonly used to simulate the welded connection between the studs and the beam flange. In the first approach a tie constraint between

the studs and the beam flange is applied [4,9]. The potential drawbacks of this method are that the connection behaviour may not be accurately captured at high deformations, the constrained nodes may be sensitive to the specified position tolerance and degrees of freedom at the root of the stud may be unrealistically constrained. The second approach is to model the studs and beam as a continuous merged part [5-8]. This is a simpler approach which may better capture the connection between the stud and the beam, but may require manual meshing if there is a large discrepancy in stud and beam mesh sizes. Some studies also explicitly model the weld collar at the root of the stud, again with either a tied constraint [9] or as part of a merged part [5,6,8], but this adds complexity to the modelling process with regard to meshing and contact definitions. An embedded constraint feature in ABAQUS is commonly used to model the interaction between the reinforcement bars and the slab, where the nodal translational degrees of freedom of the embedded (reinforcement bars) elements are constrained to the

interpolated values of the corresponding degrees of freedom of the host (concrete slab) elements.

2.4. Analysis solver

Most approaches use the Dynamic Explicit solver to overcome convergence issues due to the complex geometry and contact formulations involved in the analyses. This requires care when defining the loading rate, time incrementation and mass scaling, and kinetic and internal energy must be monitored throughout the analysis to ensure it remains quasi-static. For these reasons, the study by Katwal et al. [7] chose to use the Standard Dynamic Implicit solver, although the analysis was still sensitive to loading rate and amplitude. Alternatively, Lam and Ellobody [10] used the Standard RIKS algorithm due to its advantages for predicting unstable and nonlinear responses, while Li et al. [8] used the Standard General Static solver.

2.5. Concrete and steel constitutive models

For the concrete slab, all of the models in Table 1 except for Lam and Ellobody [10] used ABAQUS concrete damaged plasticity (CDP) material model. Material plasticity and damage evolution are defined separately for compressive and tensile behaviour. The CDP model requires five parameters to be defined, which are flow potential eccentricity e (with a default value of 0.1), ratio of biaxial to uniaxial compressive strength f_{b0}/f_{c0} (with a default value of 1.16), ratio of second stress invariants on tensile and compressive meridians K (with a default value of 0.667), dilation angle ψ and viscosity parameter μ_{visc} . The first three of these parameters are left to the default value in the literature models. The dilation angle ψ , which relates to the volumetric change of the concrete under severe plastic deformation [22], was typically taken as $30-40^{\circ}$ [7,8,11,13], though variations exist, such as Xu et al. [5], who modelled lightweight concrete and specified 53° and Kruszewski et al. [6], who model UHPC and specified 17°. The viscosity parameter μ_{visc} controls viscoplastic regularisation, which can be used to overcome instability in the analysis caused by excessive distortion and softening behaviour of the concrete [22], particularly when using the ABAQUS/Standard solver. Theoretically, μ_{visc} should be equal to zero, but a higher value may be employed to improve convergence, provided it does not affect the accuracy of the analysis results, which should be verified through a sensitivity study. Kruszewski et al. [6] and He et al. [13], who used the Dynamic Explicit analysis solver, set μ_{visc} to 0, while Katwal et al. [7] and Li et al. [8], who used the Standard analysis solvers, set μ_{visc} to 0.0001 and 0.0015, respectively.

The plastic behaviour of concrete is modelled by defining the compressive and tensile stress-strain or stress-displacement behaviours as well as their respective damage evolution. The compressive stressstrain behaviour was most commonly based on the model by Carreira and Chu [23] with linear elastic behaviour up to $0.4f_c$, followed by a nonlinear response up to the peak compressive stress f_c , as illustrated by Fig. 2(a). Variations on the post-peak softening behaviour have been proposed, such as by Pathirana et al. [4], as shown in Fig. 2(a), or by He et al. [13], where a linear softening response to a stress of $0.85 f_c$ was adopted. For the compressive behaviour shown in Fig. 2(a), the compressive stress σ_c as a function of the compressive strain ε_c is given by Eqs. (1)–(4), where E is the concrete elastic modulus and ε'_{a} is the nominal ultimate strain which is taken as 0.00175. The compressive damage evolution was commonly specified by the relationship given in Eq. (5), where d_c is the compressive damage parameter, as shown in Fig. 2(b).

$$\sigma_c = E\varepsilon_c \qquad \sigma_c \le 0.4f_c \tag{1}$$

$$\sigma_{c} = \frac{f_{c} \gamma \frac{\varepsilon_{c}}{\varepsilon_{c}'}}{\gamma - 1 + \left(\frac{\varepsilon_{c}}{\varepsilon_{c}'}\right)^{\gamma}} \qquad 0.4 f_{c} < \sigma_{c} \le f_{c}$$
(2)

$$\gamma = \left(\frac{f_c}{32.4}\right)^3 + 1.55\tag{3}$$

$$\sigma_c = \frac{f_c \varepsilon_c'}{\varepsilon_c} \qquad \varepsilon_c \ge \varepsilon_c' \tag{4}$$

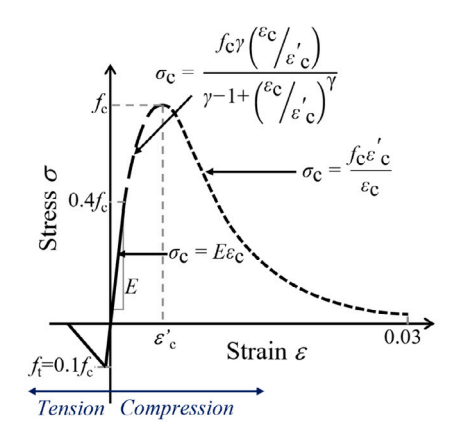
$$d_c = 1 - \frac{\sigma_c}{f_c} \tag{5}$$

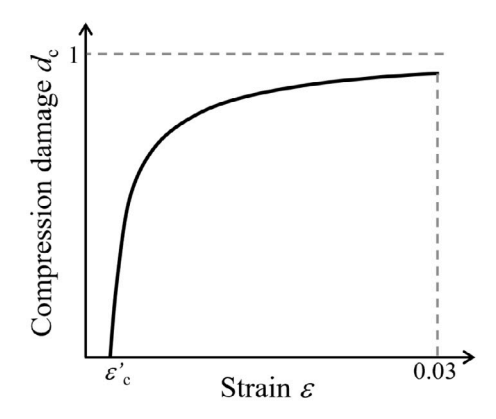
The tensile stress–strain behaviour of concrete was commonly defined as linear elastic up to a maximum tensile stress f_t equal to $0.1f_c$, followed by a linear [4,9,11,12] or non-linear [5,7,8,13] softening behaviour. Fig. 2(a) illustrates the linear softening behaviour as a function of tensile strain, but in ABAQUS the tensile behaviour may also be expressed in terms of crack displacement or fracture energy. Tensile damage evolution was not always specified, since concrete crushing is more critical in push-out tests, but where it was included it followed the same relationship as Eq. (5), where tensile damage parameter $d_t = 1 - \sigma_t/f_t$, where σ_t is the tensile stress and f_t is the maximum tensile stress.

For the steel components (beam, studs and reinforcing bars), five different plasticity models have been used, namely elastic-plastic, elastic-plastic-linear hardening, elastic-plastic-non-linear hardening, elastic-linear hardening and fully non-linear response. Pathirana et al. [4] modelled the studs as elastic-linear hardening, the beam as elasticplastic-linear hardening and the reinforcement as elastic-plastic. Xu et al. [5] and Li et al. [8] modelled all steel components as elastic-linear hardening. Kruszewski et al. [6] and Pavlovic et al. [11] modelled the beam and study using a non-linear relationship obtained from coupon tests, while the latter additionally modelled the reinforcement using a simple linear elastic relationship. Katwal et al. [7] modelled all steel components with an elastic-plastic-non-linear hardening relationship. Zhou et al. [9] modelled push-out tests where all steel components were made from stainless steel, and therefore used coupon test data to define the non-linear plastic behaviour of all stainless steel components. Lam and Ellobody [10] modelled the beam and studs using elasticplastic relationships. Tzouka et al. [12] used coupon data to model the non-linear stud behaviour while the beam was modelled with an elastic-plastic-non-linear hardening response and the reinforcement was defined as elastic-plastic. He et al. [13] also modelled the studs using non-linear behaviour obtained from coupon tests, and the beam and reinforcement were defined as elastic-plastic.

Six of the ten modelling studies summarised in Table 1 incorporated damage models for the studs. Katwal et al. [7] implicitly modelled the post-peak softening behaviour in the material plasticity definition. Xu et al. [5] used the Lemaitre continuous damage mechanics model, while the rest used a ductile damage model called the stress-modified critical strain (SMCS) model, which is based on the void growth model (VGM) developed by McClintock [24] and Rice and Tracey [25]. The plastic material model for the stud can be split into two parts: firstly, the stress-strain response up to ultimate stress, and secondly post-peak behaviour. Up to the ultimate stress, the engineering stress s and strain e, measured from tensile coupon tests, are converted to true stress σ and true plastic strain ε_{pl} using Eqs. (6)–(8), where E is the Young's Modulus. After the ultimate stress, these stress-strain equations are no longer valid, and a different approach must be taken to model the postpeak stress-strain behaviour of the stud material. Two methods from the literature incorporating ductile damage models for modelling the stud behaviour are outlined here. The first is the SMCS model used by Pavlovic et al. [11] with strain localisation and the second is the Bao-Wierzbicki (BW) model [19], as described in Song et al. [18], in addition to the weighted average method. While the study by Song et al. [18] did not model push-out tests, it described a thorough ductile damage modelling procedure for bolts in tension and shear, which can be applied to welded studs in push-out tests.

$$\sigma = s(1+e) \tag{6}$$





- (a) Compressive and tensile stress-strain curves
- (b) Compression damage evolution relationship

Fig. 2. Concrete Damage Plasticity (CDP) material model.

$$\varepsilon = \ln(1 + e) \tag{7}$$

$$\varepsilon_{pl} = \varepsilon - \frac{\sigma}{E}$$
(8)

2.5.1. Pavlovic et al. and SMCS

Pavlovic et al. [11] described a method for damage modelling of bolted and headed stud shear connectors in push-out tests. The method is presented schematically in Fig. 3(a), where point p represents the onset of plastic behaviour, n is the onset of necking, ris the onset of rupture and f is the point of complete fracture. The stress-strain response of the stud is split into individual increments i, with damage evolution parameter D_i considered at each increment i. Damage initiation is defined at the necking point n, where the damage parameter $D_n = 0$, and damage completion occurs at the fracture point f, where total damage has taken place, thus $D_f = 1$. The three components of the damage model that are input into ABAQUS are the material plasticity, damage initiation and damage evolution. The material plasticity is input as the undamaged true stress σ as a function of true localised plastic strain $\varepsilon_{pl,loc}.$ Since after necking, strains become localised in the necked region, the standard equations for converting engineering stress and strain to true stress and strain are no longer valid after the ultimate stress point n. Pavlovic et al. captured this strain localisation by adjusting the gauge length in the post-necking strain calculations at each increment i, as shown in Fig. 3(a) and given by Eq. (9), where l_0 is the original gauge length, l_{loc} is the average necking zone length, Δl_i is the incremental displacement, Δl_n and Δl_r are the incremental displacements at necking and rupture, respectively and α_L is a material factor. A post-necking engineering strain is then calculated from Eq. (10), which is converted to true plastic strain according to Eqs. (7) and (8). Undamaged true stress σ , beyond the necking point, is calculated from Eq. (11), which is similar to Eq. (6) except that s_n represents the engineering stress at the necking point (i.e., ultimate engineering stress).

$$l_i = l_0 + \left(l_{loc} - l_0\right) \left(\frac{\Delta l_i - \Delta l_n}{\Delta l_r - \Delta l_n}\right)^{\alpha_L} \tag{9}$$

$$e_i = e_{i-1} + \frac{\Delta l_i - \Delta l_{i-1}}{l_i} \tag{10}$$

$$\sigma_i = s_n \left(1 + e_i \right) \tag{11}$$

The damage initiation is set at the necking point n and is input as equivalent plastic strain at onset of damage $\varepsilon_{pl,0}$ as a function of stress triaxiality, η , which is the ratio of hydrostatic stress to Von Mises stress, given by Eq. (12), which is the SMCS relationship, where $\varepsilon_{pl,n}$ is the

equivalent plastic strain at the onset of damage for uniaxial tension (i.e., at the necking point) and β is a material parameter, taken as 1.5. This relationship is shown in Fig. 3(b).

$$\epsilon_{pl,0} = \epsilon_{pl,n} e^{-\beta \left(\eta - \frac{1}{3}\right)} \tag{12}$$

Finally, damage evolution defines the amount of damage that occurs as displacement increases i.e., the rate of stiffness degradation. The damaged stress $\sigma_{d,i}$ is calculated from Eq. (13), where s_i and e_i are the post-necking engineering stress and strain at increment i, respectively. It should be noted that this is a continuation of the standard conversion from engineering to true stress (Eq. (6)), beyond the necking point. The ratio of damaged stress $\sigma_{d,i}$ to undamaged stress σ_i is used to calculate the incremental damage evolution parameter, D_i , in Eq. (14), where α_D is a material parameter. The damage parameter D_i is input into ABAQUS as a function of the equivalent plastic displacement, $u_{pl,i}$, which is the displacement of the individual mesh elements in the model rather than the overall coupon displacement, and may be obtained from Eqs. (15)–(18). In Eqs. (15)–(18), $\varepsilon_{pl,i}$, $\varepsilon_{pl,n}$ and $\varepsilon_{pl,f}$ are the plastic strains at increment i, at necking point n and at fracture point f, $u_{pl,f}$ is the plastic displacement at fracture point, λ_S is the element size factor, L_E is the element size, L_R is the element size of the reference mesh, L_{char} is the characteristic element length and λ_E is the element type factor, which can be taken as 1 for C3D4 elements, and between 2.5 to 3.2 for C3D8R elements depending on material ductility. The damage evolution relationship is shown in Fig. 3(c).

$$\sigma_{d,i} = s_i \left(1 + e_i \right) \tag{13}$$

$$D_{i} = \begin{cases} \alpha_{D} \left(1 - \frac{\sigma_{d,i}}{\sigma_{i}} \right) & n \leq i \leq r \\ 1 & i = f \end{cases}$$
 (14)

$$u_{pl,i} = \frac{u_{pl,f} \left(\varepsilon_{pl,i} - \varepsilon_{pl,n}\right)}{\varepsilon_{pl,f} - \varepsilon_{pl,n}} \qquad i \ge n$$
(15)

$$u_{pl,f} = \lambda_s L_{char} \left(\varepsilon_{pl,f} - \varepsilon_{pl,n} \right) \tag{16}$$

$$\lambda_s = \sqrt[3]{\frac{L_R}{L_E}} \tag{17}$$

$$L_{char} = \lambda_E L_E \tag{18}$$

Pavlovic et al. incorporated an additional ABAQUS shear damage definition to model the damaged behaviour of the studs under shear loading. Similar to the tensile ductile damage models, the shear damage model consists of three key parts: plasticity, damage initiation and damage evolution. For the plasticity data, the plastic material properties

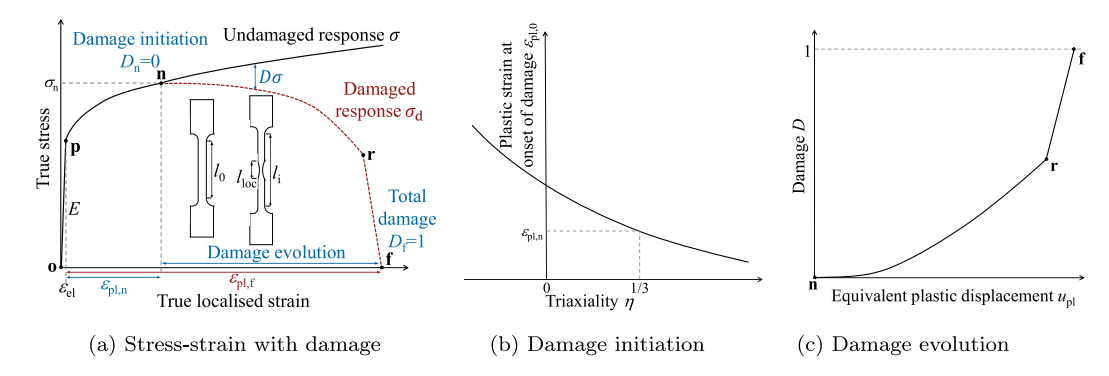


Fig. 3. Stress-strain relationship with damage initiation and evolution from Pavlovic et al. [11].

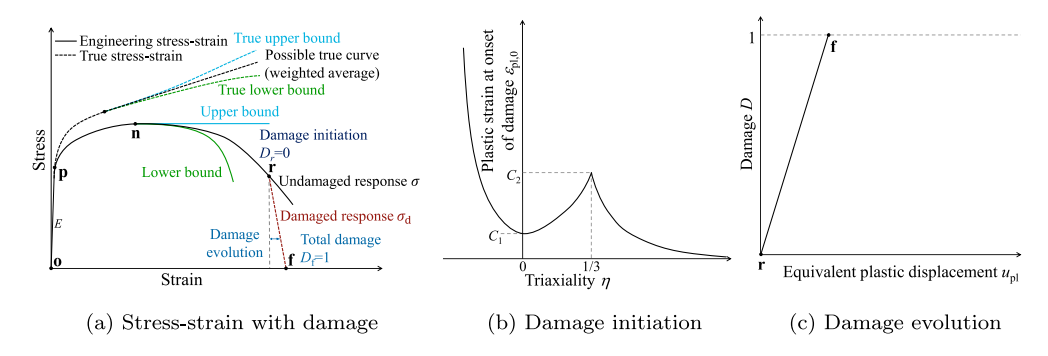


Fig. 4. Stress-strain relationship with damage initiation and evolution from Song et al. [18].

from the tensile model are used. The damage initiation is defined by shear strain at onset of damage, which is calibrated by trial and error, shear stress ratio, which is assumed to be 1.732, and strain rate, which is set to 0, and the shear damage evolution is defined by a single value of displacement at failure.

Although this ductile damage model has been implemented in the literature, it has limitations, particularly regarding its accuracy at lower triaxialities, thus requiring an additional shear damage definition to capture fracture under combined tensile-shear and shear only loading conditions. The strain localisation and damage evolution calculations require several material- and mesh-specific parameters to be calibrated, which is time consuming. Furthermore, by defining the damage initiation point as the necking point n, the model is very sensitive to the damage evolution definition, which is also complex.

2.5.2. Song et al. weighted average & Bao-Wierzbicki (BW)

The method outlined by Song et al. [18], illustrated schematically in Fig. 4(a), has four key differences to the method used by Pavlovic et al. described in Section 2.5.1. Firstly, the weighted average method proposed by Ling [26] is used to obtain the post-necking true stressstrain response from the engineering stress-strain response. Secondly, the point of damage initiation is specified at the rupture point r, rather than at the necking point n. Thirdly, the Bao–Wierzbicki (BW) relationship [19] is used to define the plastic strain at the onset of damage, which is more accurate at lower triaxialities, including under shear loading. Finally, damage evolution is defined by a single, very small value of equivalent plastic displacement to fracture. The calibration of this model requires developing an FE model of the coupon specimen, where the stress-strain data in the pre- and post-necking stages in terms of true stress and strain are defined. The pre-necking output true stressstrain data from the model should match the input data provided, while for the post-necking stage, a trial and error approach is used until the FE output agrees with coupon test data, as described hereafter.

The weighted average method [26] assumes an upper and lower bound for the post-necking true stress-strain curve which provides an envelope within which the actual stress–strain curve lies, as shown in Fig. 4(a). The upper bound corresponds to the perfect-plastic extension of the engineering curve after the necking point, calculated by Eq. (19), while the lower bound is estimated using a power law relationship, as given by Eq. (20), where σ_n and ε_n are the true stress and strain at necking, respectively. The best approximation of the true stress–strain curve lies between these bounds and is calculated using Eq. (21) with a weighted average factor, w, and when w=1 the curve follows the upper bound and when w=0, it follows the lower bound. For stainless steels, Song et al. adopted Eq. (22) for w, which varies with strain and includes two additional parameters, a_1 and a_2 , calibrated by trial and error until an acceptable agreement is reached between the test and the FE analysis results.

$$\sigma_{upper} = \sigma_n e^{\varepsilon - \varepsilon_n} \tag{19}$$

$$\sigma_{lower} = \sigma_n \left(\frac{\varepsilon}{\varepsilon_n}\right)^{\varepsilon_n} \tag{20}$$

$$\sigma = \sigma_n \left[w e^{\varepsilon - \varepsilon_n} + (1 - w) \left(\frac{\varepsilon}{\varepsilon_n} \right)^{\varepsilon_n} \right] \qquad 0 \le w \le 1$$
 (21)

$$w = \frac{1}{1 + a_1 \left(\varepsilon - \varepsilon_n\right)^{a_2}} \tag{22}$$

Damage initiation is defined using the Bao-Wierzbicki [19] model, as shown in Fig. 4(b), where the relationship between the plastic strain at onset of damage, $\epsilon_{pl,0}$, and the triaxiality, η , is defined over the full triaxiality ranges, covering shear, combined shear and tension and tensile failures as given by Eq. (23), where C_1 and C_2 are plastic fracture strains at pure shear ($\eta=0$) and pure tension ($\eta=1/3$), respectively. The C_2 parameter is calibrated first using the results of the FE coupon tensile model, by integrating the equivalent plastic strain PEEQ and triaxiality for all integration points within a critical element (Eq. (24)) and C_1 is then calibrated by trial and error. Damage evolution controls the stress–strain response from point r to point f and is defined

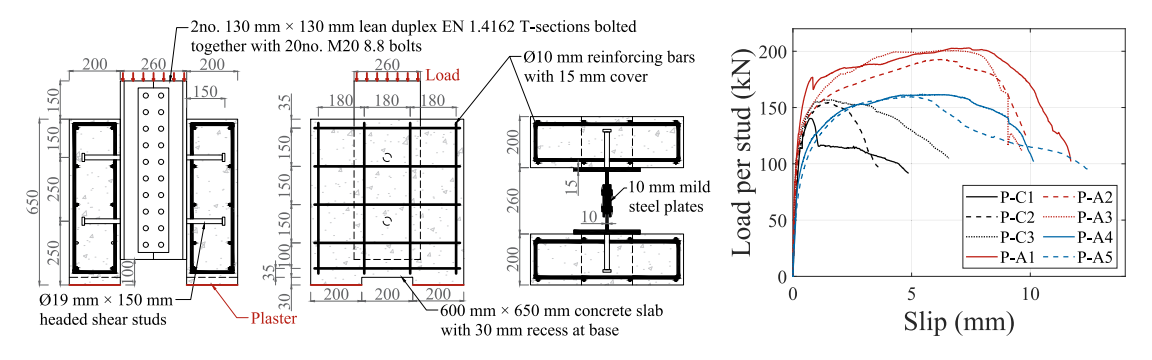


Fig. 5. Details of push-out test specimens (mm) and measured load-slip responses.

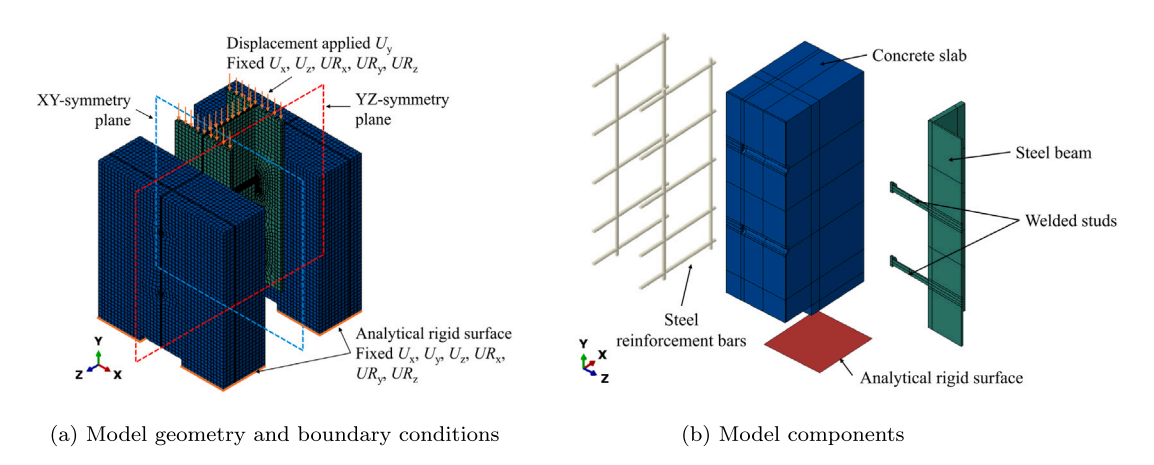


Fig. 6. Diagram of push-out model assembly and boundary conditions.

by a single, very small value of equivalent plastic displacement to fracture, illustrated in Fig. 4(c).

fracture, illustrated in Fig. 4(c).

$$D_{i} = \begin{cases} \infty & \eta \leq -\frac{1}{3} \\ \frac{C_{1}}{1+3\eta} & -\frac{1}{3} < \eta \leq 0 \\ C_{1} + \left(C_{2} - C_{1}\right) (3\eta)^{2} & 0 < \eta \leq \frac{1}{3} \\ \frac{C_{2}}{\eta} & \eta \geq \frac{1}{3} \end{cases}$$

$$C_{2} = \int \eta d\varepsilon_{pl}$$
(23)

The limitations of the method used by Song et al. are that the

(24)The limitations of the method used by Song et al. are that the

weighted average method requires several iterations to calibrate the parameters a_1 and a_2 . On the other hand, this allows the onset of damage to be defined at the rupture point r, which makes the model less sensitive to the damage evolution definition, which can be a simple linear relationship. The calculation of C_2 and subsequent calibration of C_1 require iterative trial and error, which is time consuming. However, the Bao-Wierzbicki damage initiation criteria is more accurate across a broader range of triaxialities and does not require additional shear damage to be defined separately in ABAQUS.

3. Development of FE models and validation

3.1. Push-out tests

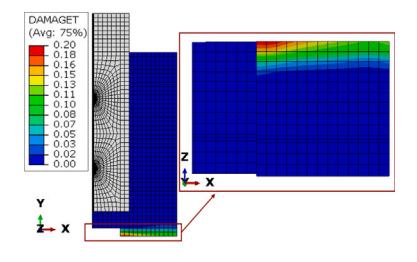
The FE models in this study were validated against push-out tests by Presswood et al. [16]. The geometry of the specimens and the measured load-slip responses are shown in Fig. 5. The key test parameters are reported in Table 2, where P_{μ} is the maximum load per shear connector, P_{Rk} is the characteristic resistance, k_{sc} is the shear connector stiffness, δ_{ke} is the elastic slip, δ_u is the stud slip capacity and δ_{uk} is the characteristic stud slip capacity ($\delta_{uk} = 0.9\delta_u$). The beams were fabricated from lean duplex EN 1.4162 stainless steel plates, with either carbon steel ($f_u = 500$ MPa) or austenitic EN 1.4301 stainless steel $(f_u = 692 \text{ MPa})$ studs welded to the flanges of the beams. All studs had a diameter of 19 mm and a total height of 150 mm. Specimens P-C1 to P-C3 and P-A1 to P-A3 used high-strength C100 concrete, while specimens P-A4 and P-A5 used medium strength C50 concrete. The concrete slabs were embedded in dental plaster to fix them to the base of the test machine, and load was applied to the top surface of the beam. Aluminium shims and a thin rubber sheet were used to make sure the load was applied evenly. All the push-out specimens failed at the stud root with little concrete damage. Presswood et al. [16] also describe tensile coupon tests and double shear tests on material cut from the shanks of the welded shear studs, the results of which are used herein for development of stud damage models. Two different approaches to damage modelling are presented and compared, both based on the Bao-Wierzbicki method.

3.2. Geometry and mesh

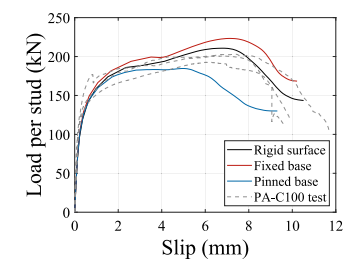
The push-out tests were modelled using the FE package ABAQUS/Standard with static general analysis. The use of explicit analysis solver was considered; however, it is highly sensitive to mass scaling, making accurate validation particularly challenging. In contrast, the static general analysis avoids this and is a straightforward and reliable approach. By appropriately defining assembly partitions, meshing, contact formulations and viscosity, convergence issues could be avoided. The model exploited the symmetry of the test by modelling one quarter of the specimen to reduce computational time. Fig. 6(a) shows a mirrored view of the model which represents the whole specimen and Fig. 6(b) shows the components of the quarter-model. The studs were welded to the beam thus the two components were modelled as merged part, and the welds were not explicitly considered during the analysis. The 10 mm reinforcing bars were modelled as wire truss elements using a 30 mm T3D2 mesh. All other components used

Table 2
Results of push-out tests

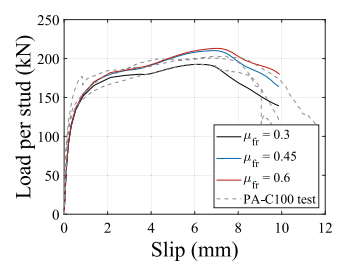
Stud material	Concrete grade	Specimen	$P_{\rm u}$ (kN)	$P_{\rm Rk}$ (kN)	k _{sc} (kN/mm)	δ_{ke} (mm)	$\delta_{\rm u}$ (mm)	$\delta_{\rm uk}$ (mm)	FE model name
	C100	P-C1	141	127	444	0.30	-	_	PC-C100
		P-C2	154	139	416	0.33	2.6	2.3	
Carbon steel		P-C3	157	141	549	0.26	4.2	3.8	
		Mean	151	136	470	0.30	3.4	3.1	
	C100	P-A1	203	183	533	0.30	9.4	8.5	PA-C100
		P-A2	193	174	271	0.64	8.7	7.8	
A		P-A3	201	181	282	0.64	8.5	7.7	PA-C100
Austenitic EN 1.4301		Mean	199	179	362	0.53	8.9	8.0	
EN 1.4301		P-A4	162	146	255	0.57	8.6	7.7	_
	C50	P-A5	160	144	201	0.71	6.7	6.0	PA-C50
		Mean	161	145	228	0.64	7.7	6.9	



(a) Concrete tension damage at the base of the slab with fixed boundary conditions



(b) Effect of different boundary conditions on PA-C100 push-out model



(c) Sensitivity of push-out model to different friction coefficients μ_{fr} at the slab base surface

Fig. 7. Effect of different boundary conditions at base of slab.

solid C3D8R mesh elements; the slab and the beam had a mesh size of approximately 15 mm and the studs had a mesh size of 1.5 mm, which was chosen following a mesh sensitivity study which is described in Section 3.5.1. The models need to be carefully partitioned to maintain mesh sizes close to the specified values in case of parametric studies, where the sizes of the model elements e.g., stud height may be changed.

3.3. Boundary conditions and interactions

Symmetry boundary conditions were applied to the beam web and the inner faces of the beam, studs and slab, corresponding to the XY and YZ planes of symmetry as shown in Fig. 6(a). The load was applied via displacement $U_{\rm v}$ at the beam top; all other degrees of freedom were fixed to replicate the experimental test setup, which used a fixed plate to apply the test load. As explained in Section 2.1, an analytical rigid surface beneath the slab was modelled to replicate the boundary conditions of the experimental test; the rigid surface was fully fixed, and hard contact with suitable friction coefficient μ_{fr} was defined between the top of the rigid surface and the bottom of the slab. This was found to most accurately replicate the experimental test boundary conditions. When a fully fixed boundary condition was applied directly to the slab, this caused tension damage in the base of the slab due to the moment caused by the loading in conjunction with the slab recess, as illustrated in Fig. 7(a). The damage at the base could be avoided by applying pinned boundary conditions, however this did not replicate the test conditions and led to an underprediction of the push-out capacity, as shown in Fig. 7(b).

A sensitivity study was carried out to verify the friction coefficient μ_{fr} , comparing values from 0.3 to 0.6, and the results are presented in Fig. 7(c). A value of 0.45 was found suitable, which is consistent with the value used for steel and grout contact by Gomez [27]. Surface-to-surface contact was defined for the contact between the steel (flange and studs) and concrete, using hard contact definition with μ_{fr} of 0.4

and small sliding. A value of 0.4 is typically used in the literature [4,6, 8,9,13] for steel–concrete contact friction, as discussed by Gomez [27]. An embedded constraint was applied to the reinforcement bars within the concrete slab. To plot the load-slip responses, relative slip was calculated from the difference between the output displacements of a beam node and slab node, close to one of the studs, and load was taken from the output forces of the reference point on the slab rigid surface.

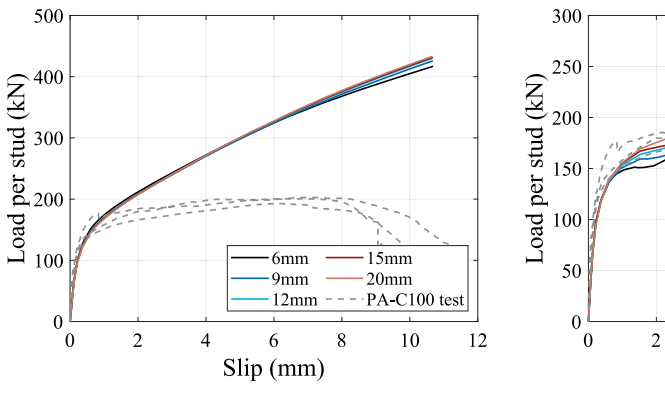
3.4. Concrete material modelling

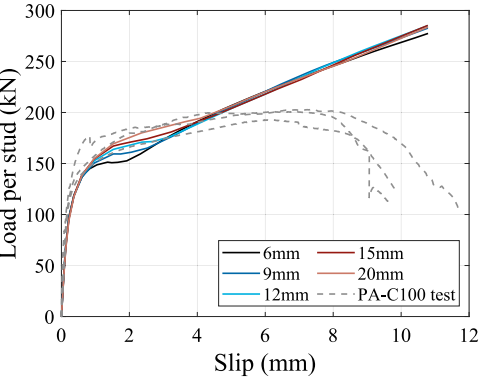
The concrete material model was defined using concrete damaged plasticity (CDP) in ABAQUS. Elastic behaviour was defined using Young's Modulus, E, as per Eq. (25) [28], where ρ_c is the concrete density of 2400 kg/m³, f_c is the compressive strength and v is the Poisson's ratio of 0.15. Compressive behaviour, including damage, was defined using Eqs. (1)-(5) presented in Section 2.5 and illustrated in Fig. 2. The tensile behaviour of the concrete was defined using a linear stress-displacement relationship with tensile strength f_t taken as $0.1f_c$. The maximum value of crack displacement u was calculated from the fracture energy, G_f , in N/mm, according to Eq. (26), since G_f corresponds to the area underneath the stress-displacement curve, and was calculated from Eq. (27) according to CEB-FIP Model Code 2010 [29]. Tensile damage d_t was defined as 0 at zero displacement and 0.95 at maximum displacement u, to avoid a sudden drop in the stress at the material point, which can cause dynamic instability and convergence issues.

$$E = \rho_c 0.043 \sqrt{f_c} \tag{25}$$

$$u = \frac{2G_f}{f_t} \tag{26}$$

$$G_f = 0.073 f_c^{0.18} (27)$$





- (a) No concrete or stud damage
- (b) Concrete damage but no stud damage

Fig. 8. Concrete slab mesh sensitivity results.

The CDP plastic material parameters were taken as $\psi = 40^{\circ}$, e = 0.1, $f_{b0}/f_{c0} = 1.16$ and K = 0.667. The model was very sensitive to the mesh viscosity parameter, μ_{visc} , and as discussed in Section 2.5, while increasing the value of μ_{visc} can improve convergence, the results must be carefully checked, since increasing viscosity delays the onset of damage. A sensitivity study was carried out for values of μ_{visc} from 0.005 to 0.04 to investigate the influence on the load-slip response of the push-out analysis. The elastic response and peak load were not affected, with a range of less than 2.5% between the minimum and maximum peak load from the sensitivity analysis. Discrepancy arises in the plastic transition zone (between approximately 0.5-4 mm slip), where higher values of μ_{visc} lead to steeper load-slip responses; this is because increasing the viscosity delays the onset of concrete damage. Since all models are ultimately controlled by stud failure, this discrepancy did not influence the ultimate load of the analyses. A μ_{visc} value of 0.03 was chosen for use in further analyses, which was found to best mimic the load-slip response in the plastic transition zone and achieved convergence within a manageable computational time.

The CDP material model for concrete is very mesh sensitive, so a mesh sensitivity study was carried out to help choose an appropriate mesh size. Fig. 8(a) shows the results of a mesh sensitivity study in a model containing no concrete or stud damage; the concrete slab mesh size had little effect on the push-out model response. Fig. 8(b) shows the results of a mesh sensitivity study in a model with concrete damage (damage parameters kept constant for each mesh size), but no stud damage; this shows that the mesh size had significant effect on the initial plastic region of the load-slip response, but little effect on the overall peak load, as initial concrete damage happens at low slip, then the load is redistributed and primarily taken by the stud. Ultimately, a 15 mm mesh size was chosen for the concrete slab as this gave a good match with the experimental results while maintaining computational efficiency.

3.5. Steel material modelling

The model was not sensitive to the beam and rebar material properties, since they do not contribute significantly to the capacity of the push-out specimen, hence a simple elastic-linear hardening relationship was used for both [5,8]. For the rebar, nominal material properties for grade 500 were used, while for the beam, the measured material parameters taken from the coupon tests reported in [16] were employed. Modelling the stud stress–strain behaviour would have a significant impact on the results, and therefore different approaches were employed, in particular with respect to damage modelling. Two methods are described hereafter for modelling stud damage, Method A and Method B. Both methods are based on the Bao–Wierzbicki relationship and require the calibration of damage parameters, which fully or partially rely on modelling the stud tensile and shear coupon behaviour, as described hereafter.

3.5.1. Tensile and double shear coupon models

Models of the stud coupon under tension and shear loadings were developed for the calibration of the material tensile and shear damage parameters through FE analysis. A proportional tensile coupon with a diameter of 10 mm and parallel length of 55 mm was modelled as a homogeneous solid part as shown in Fig. 9(a) [16], using C3D8R elements with 1.5 mm mesh size. A pinned restraint was applied to the top of the coupon via a rigid body reference point, likewise vertical displacement was applied to the base of the coupon.

For the stud double shear models, one quarter of the shear test geometry was modelled to reduce computational time, as shown in Fig. 9(b), using symmetry boundary conditions. The nut and the rod were modelled as a single homogeneous solid part. A fine mesh with filleted corners was required to capture the shear behaviour of the rod and to minimise the effect of stress concentrations at the interface between the shear plates. The mesh size was 1.5 mm for the rod, 1.5 mm in the plates adjacent to the rod and 2 mm elsewhere. All elements were C3D8R solid brick elements. Augmented Lagrange hard contact with a friction coefficient of 0.3 was used to define the contact between the shear plates and the rod. A pinned constraint was applied to the top of the central plate via a rigid body reference point and vertical displacement was applied to the bottom of the end plate. A very small 0.2 mm gap was introduced between the nut and end plate, to account for the fact that the nuts were only hand-tightened. For both models, the static general analysis solver was used.

Damage models are highly mesh sensitive [18], and the tensile coupon, shear and push-out models need to adopt the same mesh topology for the calibrated damage parameters to be applicable. A mesh sensitivity study was carried out to select the most appropriate mesh size. The results of the mesh sensitivity studies for the tensile and shear models are presented in Fig. 10, with mesh sizes ranging from 1–4 mm with constant material and damage properties. A mesh size of 1.5 mm was chosen as it gave good accuracy in both tensile and shear models.

3.5.2. Method A: Ductile damage model using stud tensile and shear coupon test data

Since the Bao-Wierzbicki (BW) fracture strain-triaxiality relationship can capture a wide range of triaxialities, as shown in Fig. 4(b), it was used as the basis for the ductile damage models in this study. A single ductile damage model was therefore calibrated, with the C_1 parameter calibrated from shear test results and C_2 from tensile coupon results. Damage initiation was set at the rupture point r. An accurate material plasticity model was required to represent the softening of the tensile curve from point r to point r, followed by damage evolution from r to f, as shown in Figs. 4(a) and Fig. 4(c). A simplified version of the weighted average method was adopted, whereby the true stress-strain curve was extended linearly beyond the necking point, and the

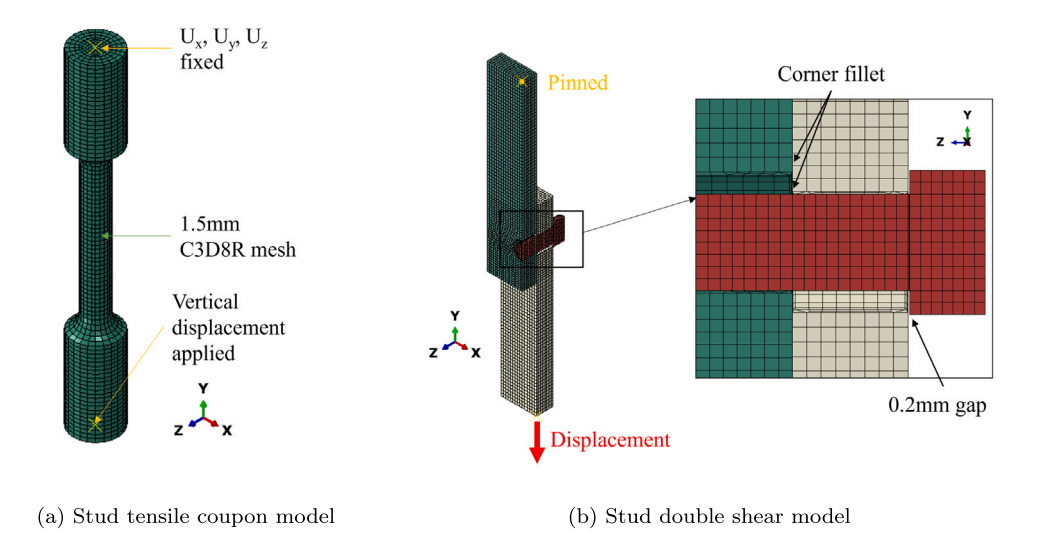


Fig. 9. ABAOUS FE models of tensile and double shear stud coupons.

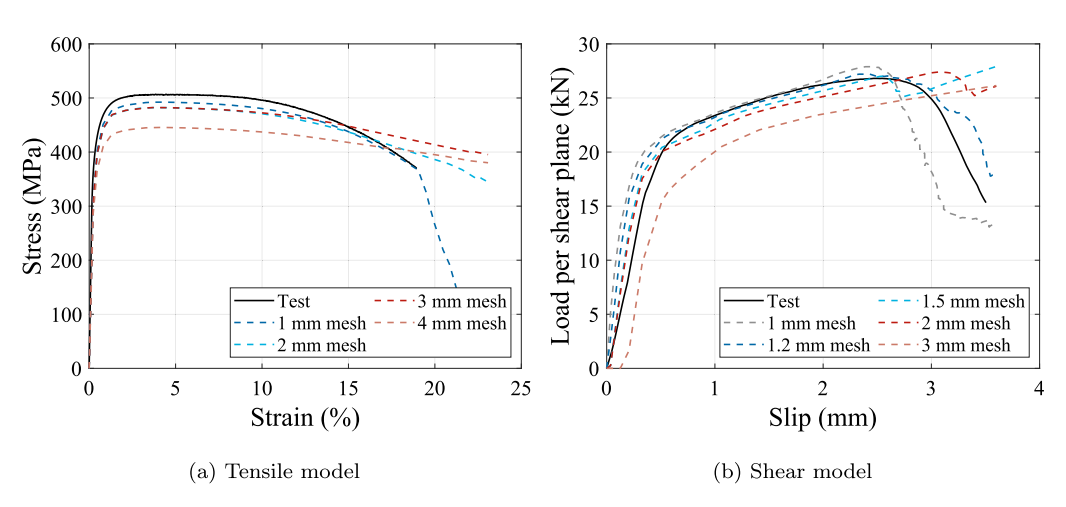


Fig. 10. Mesh sensitivity results for tensile and shear models.

slope of the extension was adjusted by trial and error until a good fit between the FE and experimental stress–strain data was obtained.

For the damage initiation definition, C_2 was calibrated first against tensile coupon test data through trial and error, using a single data point for damage initiation corresponding to a triaxiality of 1/3. The whole BW relationship was then input into the FE shear model, fixing C_2 as the calibrated value from the tensile model, but varying C_1 until a good agreement between the FE and experimental shear load-slip curve was obtained. Damage evolution in the tensile model controls the part of the curve after point r where the stress suddenly decreases to zero. In the shear model, it controls the softening of the load-slip curve after the peak. Damage evolution was defined by a bi-linear relationship, specifying values of fracture displacement at 50% ($U_{f,50}$) and 90% ($U_{f,90}$) damage. These values were found by trial and error. The damage initiation and evolution parameters for Method A are given in Table 3.

3.5.3. Method B: Ductile damage model using stud tensile coupon and push-out test data

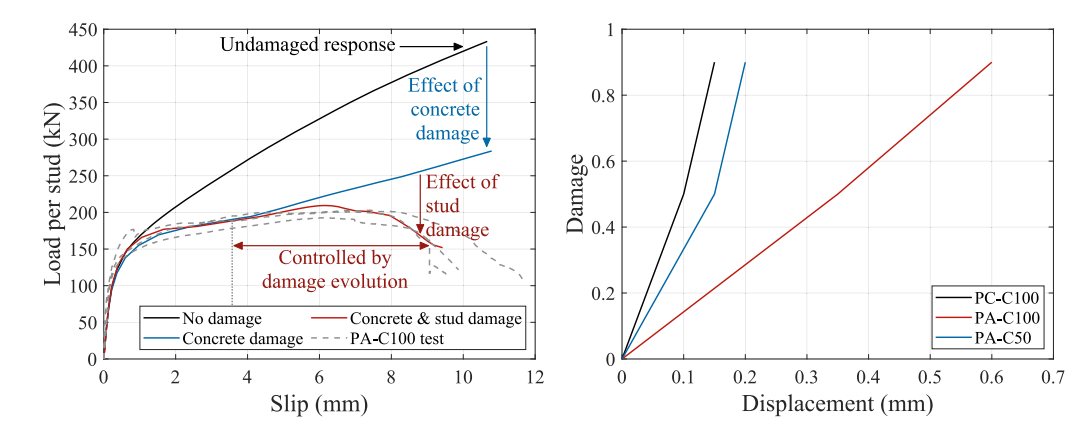
An alternative method was also used, where C_1 and damage evolution parameters were calibrated directly from the push-out test results rather than from the double shear test results. The same C_2 as calibrated in Method A was used, since the tensile material properties and mesh topology remained constant. The value of C_1 was varied until the FE

Table 3
Method A ductile damage parameters.

Stud material	Mesh size (mm)	C_1	C_2	$U_{f,50}$	$U_{f,90}$
Carbon steel	1.5	0.23	1.1	0.10	0.15
Austenitic EN 1.4301	1.5	0.25	1.2	0.06	0.09

push-out model results, employing the input material parameters, were in good agreement with the experimental load-slip curves. Damage evolution was also calibrated by trial and error to fit the push-out responses, using the same bi-linear relationship as previously. Fig. 11(a) illustrates the difference between the undamaged and damaged response from the push-out models; it is seen that both concrete damage and stud damage are required to accurately capture the load-slip response from experimental tests.

Damage evolution controls a significant portion of the push-out load-slip response, unlike the tensile model, where damage initiates at rupture and is therefore not sensitive to damage evolution. It was found that the damage evolution for the same stud material differed in different concrete strengths. In the experimental tests, the load-slip response of the austenitic stainless steel studs in C100 concrete varied significantly from the austenitic stainless steel studs in C50



(a) Effect of damage evolution on push-out model (b) Calibrated damage evolution parameters for exresponse perimental validations

Fig. 11. Damage evolution calibrated directly from push-out results.

Table 4
Method B ductile damage parameters.

Stud material	Ref	Concrete grade	Mesh size (mm)	C_1	C_2	$U_{f,50}$	$U_{f,90}$
Carbon steel	[16]	C100	1.5	0.20	1.10	0.10	0.15
Austenitic EN 1.4301	[16]	C100	1.5	0.14	1.20	0.35	0.60
Austenitic EN 1.4301	[16]	C50	1.5	0.14	1.20	0.15	0.20
Duplex EN 1.4462	[9]	C35	1.5	0.14	1.35	0.02	0.025
Duplex EN 1.4462	[9]	C70	1.5	0.14	1.35	0.35	0.40

concrete, despite the failure being governed by stud fracture. The PAC50 tests showed less ductility than the PA-C100 tests; this is due to the larger deformations in the weaker concrete, leading to bending in the stud; the combination of bending and shear stresses in the stud cause earlier fracture than under predominantly pure shear, as is the case with PA-C100. This demonstrates the complex interactions between the materials in push-out tests and highlights the need for accurate damage models for both concrete and studs, even when stud failure dominates. The damage evolution linear relationships for carbon steel studs in C100 concrete and austenitic stainless steel studs in C50 and C100 concrete are shown in Fig. 11(b). Table 4 presents a summary of the calibrated C_1 , C_2 , $U_{f,50}$ and $U_{f,100}$ parameters.

4. Validation results and discussions

4.1. Validation of presswood et al. tests

The validation results from Method A, described in Section 3.5.2, are presented in Fig. 12 for the tensile and double shear FE models. Fig. 12(a) shows that the FE tensile results align well with the experimental stress–strain curves for both carbon and stainless steel studs. In Fig. 12(b), the carbon steel double shear FE model shows a good fit with the experimental data, although the ductility is slightly overestimated. The austenitic stainless steel double shear FE model shows a reasonable fit; the model does not capture all of the strain hardening of the experiment, and underestimates the peak load by 17%; a higher value of C_1 would achieve a closer fit with the shear test data, but was found to overestimate the peak capacity and ductility of the push-out model. Fig. 12(a) also shows the failure of the coupon models just before the onset of complete fracture, which correlate well with photographs of the fractured experimental specimens and DIC strain outputs [16].

The validated push-out results from both methods are presented in Fig. 13. While Method A accurately replicates the responses for the carbon and austenitic stainless steel studs in C100 concrete, it does not do so for the austenitic stainless steel studs in C50 concrete.

For the carbon steel studs in C100 concrete, the model captures the initial stiffness very well, though it slightly over-predicts the peak load - 2.4% higher than the maximum load and 6.6% higher than the average peak load across the three tests. In terms of ductility, although the experimental results show some scatter; the model validation lies within the experimental range and is considered accurate. Similar observations are made for the austenitic stainless steel studs in C100 concrete, the peak load is 5.4% higher than the maximum load and 7.4% higher than the average peak load across the three tests. For the model with austenitic stainless steel studs in C50 concrete, only the concrete strength differs from the PA-C100 model, yet the response becomes very inaccurate. The discrepancy between the PA-C50 FE and experimental results after stud damage initiation is due to the inaccurate simulation of the stud damage evolution through Method A, as these studs experienced greater bending compared to those in C100 concrete [16]. Because the BW stud damage model in Method A is only calibrated based on values of triaxiality under pure tension and pure shear, it cannot accurately account for intermediate values of triaxiality relating to bending, which make it an unreliable method for predicting the behaviour of studs in different concrete strengths. The Method A approach is similar to bolted connection modelling, where tensile and shear parameters are separately calibrated and then combined in a full model [18]. However, this approach is inadequate for push-out modelling due to the interaction between the steel and the concrete, with more complex stress states.

In Method B, where the C_1 and damage evolution parameters are directly calibrated from push-out tests, the obtained stud damage parameters more accurately represent the real triaxiality state of the push-out specimens. As shown in Fig. 13, Method B provides excellent validation of initial stiffness, peak load and ductility for all three models. However, a drawback of this method is that the calibrated damage parameters, C_1 and damage evolution, are specific to each push-out test with different concrete strengths. Nevertheless, due to its accuracy and relative simplicity of calibration, Method B is considered sufficient for parametric studies, provided that the damage parameters

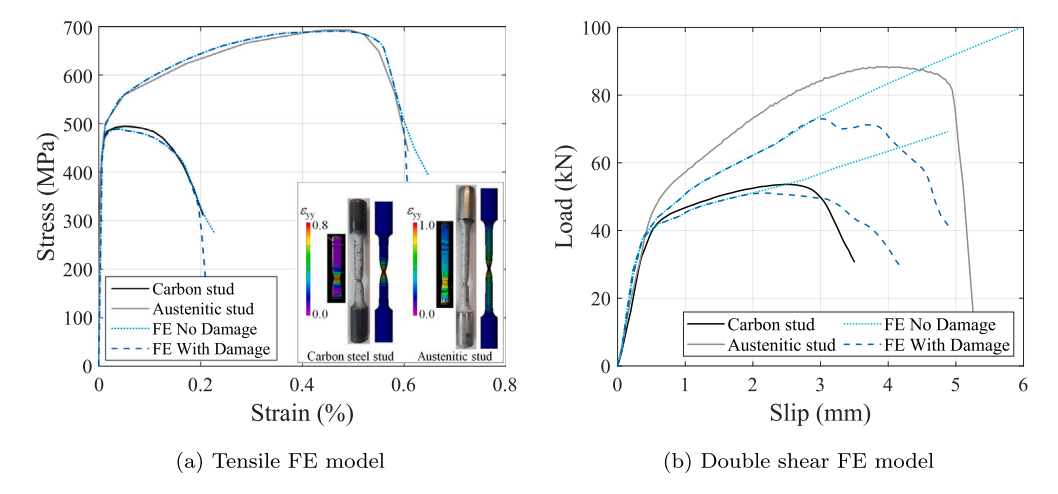


Fig. 12. Method A: tensile and shear validation results compared to experimental data.

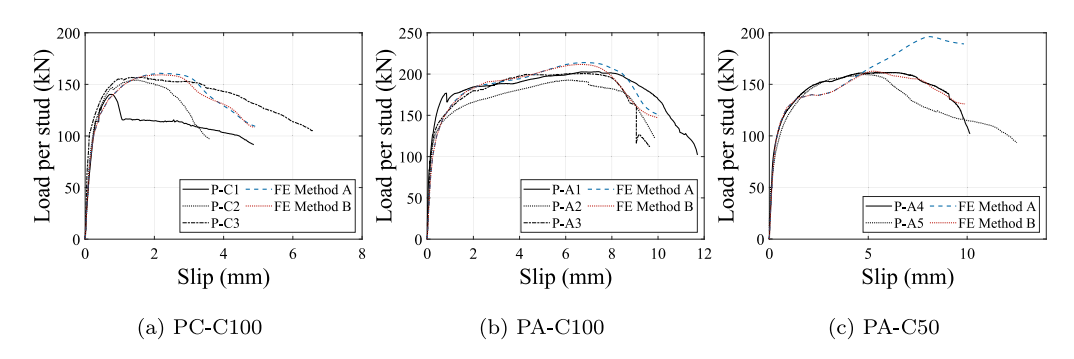


Fig. 13. Load-slip results from push-out model validations.

are calibrated for each concrete grade based on reliable push-out test data. Fig. 14 shows the damaged concrete slabs together with their corresponding concrete compression and tension damage outputs from the FE models. For all models, there is good agreement between the test and FE failure modes; the size of the concrete crushed zone below the stud agrees with the damaged area from the experimental specimens, and similar areas of tension damage are visible above the stud, where in the experimental specimens the stud has deformed, creating a gap in the concrete above.

4.2. Validation of Zhou et al. tests

The results of the push-out tests on 16 mm duplex stainless steel studs reported in Zhou et al. [9] were also validated using the Method B modelling approach described above; the ductile damage parameters are presented in Table 4. The studs were a duplex grade EN 1.4462, embedded in C70 and C35 concrete, shown as P2 and S2 in Fig. 15(a), respectively. As above, the stiffness, peak load and ductility measured from the FE models achieve a very good match with the experimental results. Similar to PA-C50, the P2 model exhibits a loss of stiffness in the early plastic stage of the load-slip response, which is due to the sensitivities of the concrete damage modelling. These validations are useful as they demonstrate that the modelling strategy adopted is applicable to different push-out configurations, including different geometric and material properties. Furthermore, they enabled the calibration of duplex EN 1.4462 stainless steel stud damage parameters, which are needed for future parametric studies.

4.3. Validation of Pathirana et al. tests

A final validation was carried out against test results presented in Pathirana et al. [4] for 19 mm carbon steel studs embedded in C40 concrete, shown in Fig. 15(b). The results from [4] were only reported up to the peak load, therefore this numerical model did not incorporate stud damage, yet is useful for further demonstrating the robustness and wide applicability of the model to different geometries and material properties. The material model for the carbon steel studs consisted of a tri-linear relationship with strain hardening. The reported failure mode by Pathirana et al. was combined concrete crushing and stud weld failure; the validated numerical model shown here demonstrated significant concrete crushing at the peak load, and only the elements at the very root of the stud exhibited excessive plastic strain above 10%; these deformations are judged small enough to not have led to damage initiation, if ductile damage was present. Therefore the modelling procedure in this paper is also applicable in tests where stud damage does not occur before the ultimate load is reached.

Table 5 provides a summary of the results from all the validation models, where the mean experimental peak load per stud $(P_{u,Exp})$ and FE peak load per stud $(P_{u,FE})$ as well as the experimental ultimate slip $(\delta_{u,Exp})$, calculated according to Eurocode 4 [1], and FE ultimate slip $(\delta_{u,FE})$ are compared. All models are within 7% of the mean experimental peak load, and 9% of the mean slip, which demonstrates excellent capability of the modelling strategy to predict the capacity and ductility of carbon steel and stainless steel shear studs in push-out tests.

4.4. Load-transfer mechanisms

The validated models were used to assess the expected load carrying mechanism in a push-out test. Considering the two load transfer mechanisms between the stud and concrete: bearing between the stud and concrete and shear between the steel and concrete, these forces were extracted from the FE models as shown in Fig. 16, where 'CFS2' represents the shear force in the *y*-direction, i.e. friction, and 'CFN2'

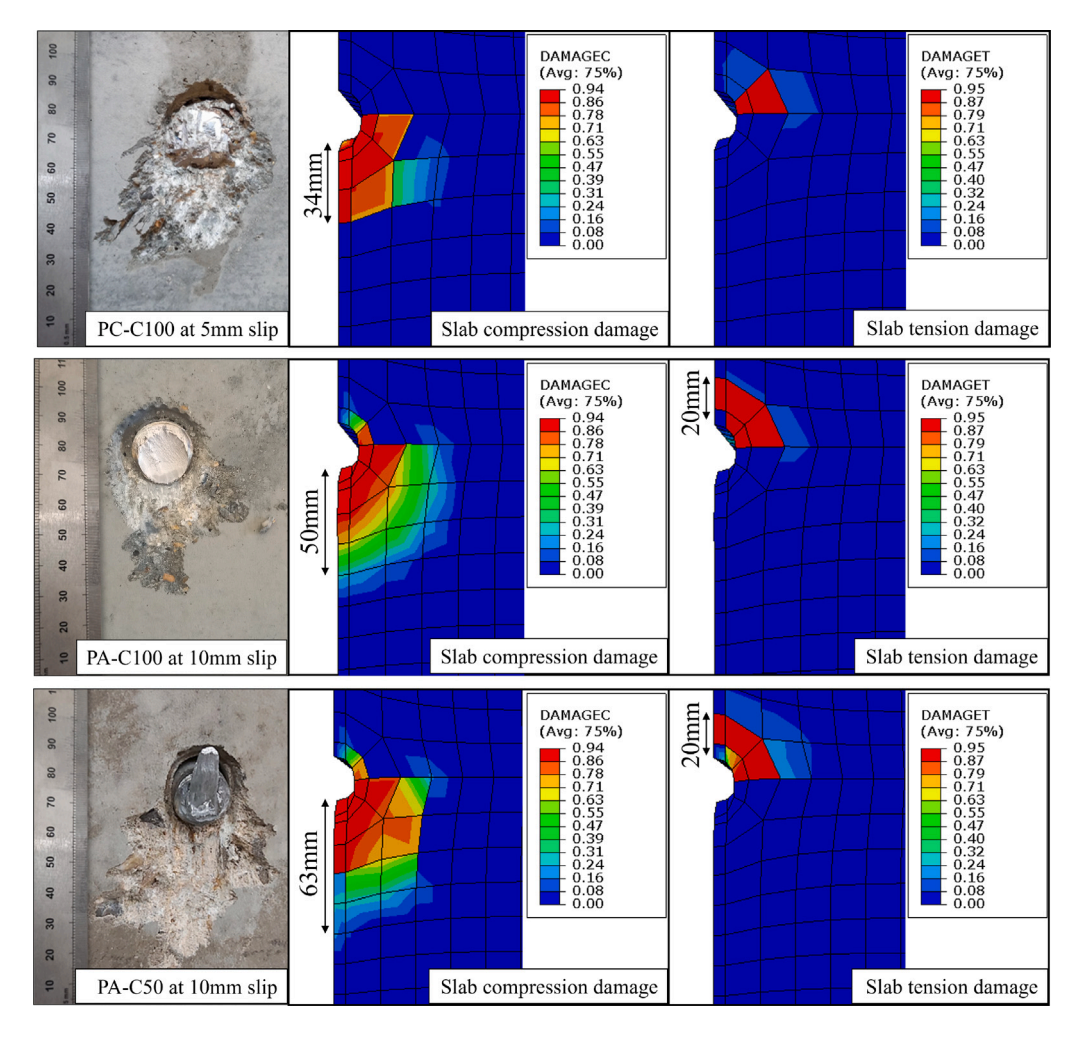
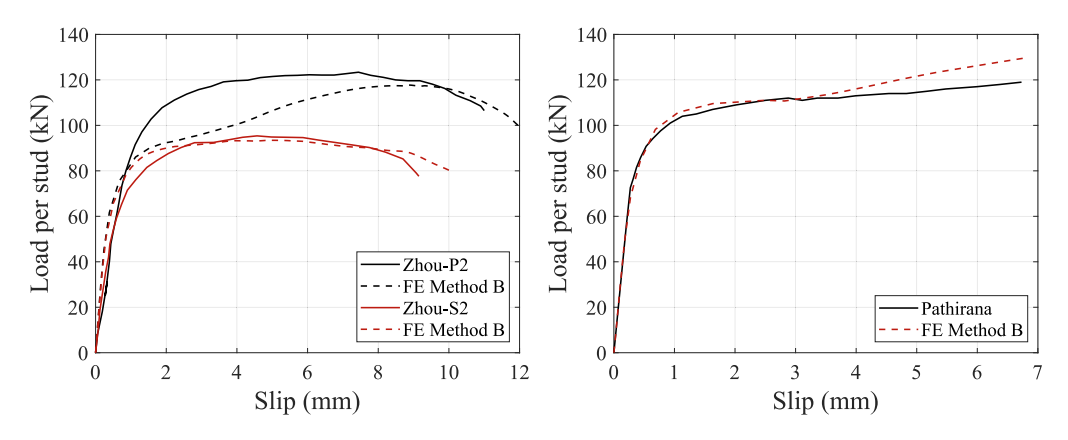


Fig. 14. Post-peak concrete damage from ABAQUS FE models compared with damaged slabs after push-out test.



(a) Zhou et al. [9] push-out tests on duplex stainless (b) Pathirana et al. [4] push-out tests on carbon steel shear studs (without stud damage)

Fig. 15. Validation of push-out tests from the literature.

represents normal forces in the *y*-direction, i.e. bearing. The force contributions are presented in Fig. 17 and show that the majority of the load is transferred by stud bearing onto the concrete and 20%–30% of the load is transferred via friction between the beam and slab, regardless of stud material or concrete strength. This proportion remains fairly

constant throughout the load duration, after an initial rapid increase in the elastic region. The majority of this friction occurs at the root of the stud. Even though the surface of the beam flange is greased before casting the concrete slab, the friction component is quite high; greasing the flange prevents any bonding between the flange and concrete slab,

Table 5
Summary of push-out test validation results.

1						
Test series	$P_{u,Exp}$ (kN)	$P_{u,FE}$ (kN)	$P_{u,FE}/P_{u,Exp}$	$\delta_{u,Exp}$ (mm)	$\delta_{u,FE}$ (mm)	$\delta_{u,FE}/\delta_{u,Exp}$
PC-C100	150.5	159.8	1.06	3.4	3.3	0.97
PA-C100	198.9	212.4	1.07	8.9	8.4	0.94
PA-C50	160.9	163.6	1.02	7.7	8.4	1.09
Zhou-P2	246.8	239.4	0.97	10.6	11.4	1.08
Zhou-S2	190.8	186.9	0.98	8.6	9.4	1.09
Pathirana	119.0	125.6	1.06	_	_	_

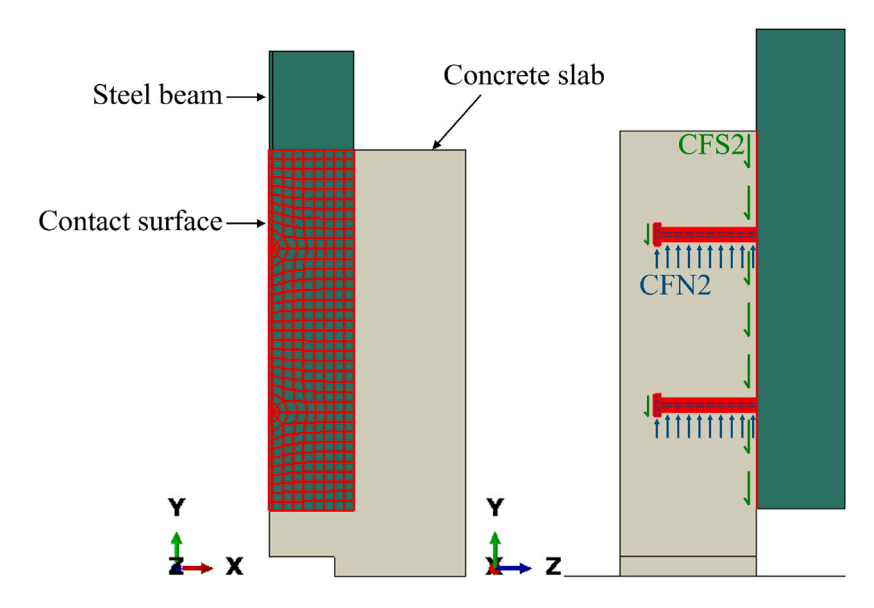


Fig. 16. Validation of push-out tests from the literature.

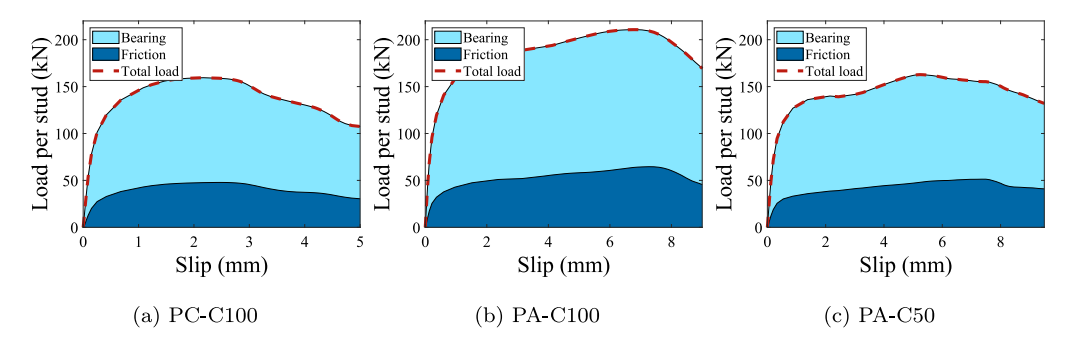


Fig. 17. Load transferred by bearing and friction in models.

but during the push-out test there is still friction due to the contact pressure between the surfaces, especially once the stud deforms.

4.5. Parametric study on stud aspect ratio

According to Eurocode 4 [1], the design resistance P_{Rd} of headed shear studs in push-out tests is determined from the minimum of Eq. (28) (governed by stud failure) and Eq. (29) (governed by concrete failure), where f_u is the stud ultimate strength, d is the stud diameter, f_c is the concrete compressive strength, E_{cm} is the concrete modulus and γ_v is the partial factor, equal to 1.25. The α factor is a reduction for studs with short aspect ratio, and is calculated from Eq. (30) where h is the stud height. Studs with h/d below 3 should not be used due to the increased likelihood of pry-out failure.

$$P_{\rm Rd,s} = \frac{0.8 f_{\rm u} \pi d^2 / 4}{\gamma_{\rm v}} \tag{28}$$

$$P_{\rm Rd,c} = \frac{0.29\alpha d^2 \sqrt{f_{\rm c} E_{\rm cm}}}{\gamma_{\rm v}} \tag{29}$$

$$\alpha = \begin{cases} 0.2(\frac{h}{d} + 1) & \text{for } 3 \le h/d \le 4\\ 1 & \text{for } h/d > 4 \end{cases}$$
 (30)

The validated model was used to conduct parametric studies on the effect of the height-to-diameter ratio h/d of the austenitic EN 1.4301 stainless steel shear connectors. The model was based on the tests by [16], with stud diameters of 16 mm, 19 mm, 22 mm and 25 mm and stud heights ranging from 35 mm to 250 mm, giving a range of h/d between 1.4 and 15.6. The results for C50 and C100 concrete are presented in Fig. 18, which shows how the ultimate load capacity of the studs varies with h/d ratio for each stud diameter, and Fig. 19, which shows the impact of h/d on the ultimate slip capacity d_u . Figs. 18 and 19 also illustrate the failure mode for each model; stud failure, concrete failure, combined stud and concrete failure, or pry-out failure. The limit for pry-out failure was found to be h/d = 1.84; studs with h/dabove this limit did not exhibit pryout failure. The load capacity and ductility of the studs both showed slight increase between $2 \le h/d \le 3$ before reaching a plateau. This suggests that the h/d limit of 3 in Eurocode 4, with a reduction factor applied for h/d between 3 and 4,

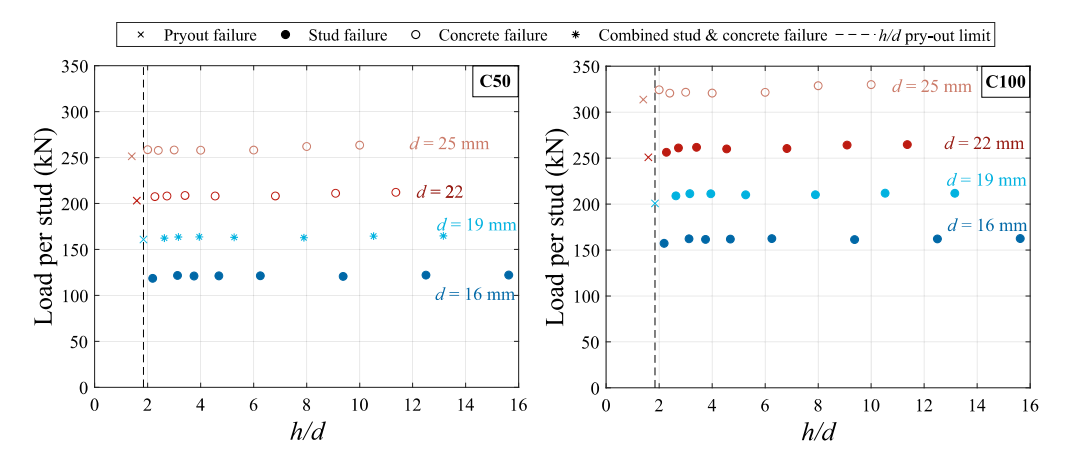


Fig. 18. Effect of h/d ratio on load capacity of austenitic EN 1.4301 stainless steel studs embedded in C50 and C100 grade concrete.

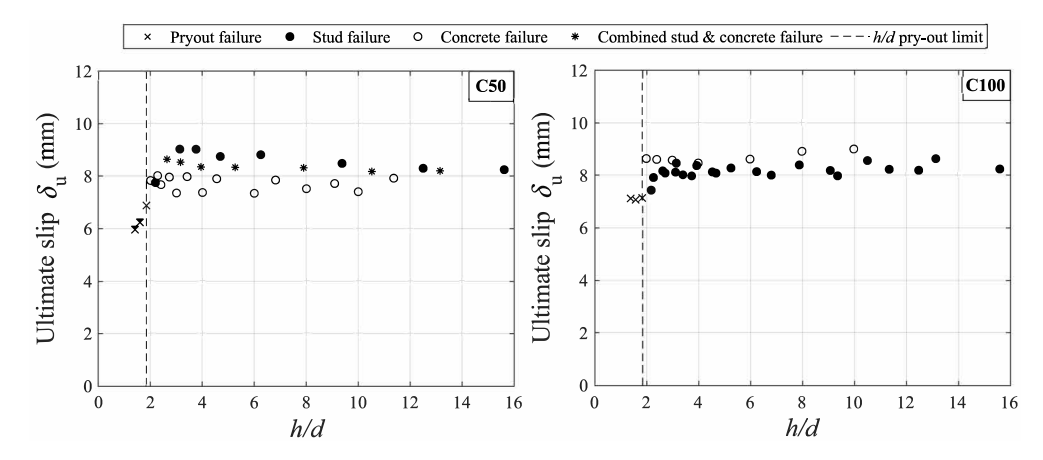


Fig. 19. Effect of h/d ratio on ultimate slip capacity of austenitic EN 1.4301 stainless steel studs embedded in C50 and C100 grade concrete.

could be relaxed. Further parametric studies including the effect of stud diameter, stud height, stud grade and concrete strength will be carried out in the future to assess the applicability of Euocode 4 to stainless steel shear studs in greater detail.

5. Conclusions

This paper investigated the numerical modelling of push-out tests with welded headed shear studs in solid slabs. A comprehensive review of existing approaches for finite element modelling of push-out tests has been presented, with a particular focus on techniques for representing the stress-strain responses of concrete and shear studs, including damage, to accurately capture the full load-slip response — an area that has received limited attention in the literature. To this end, the applicability of the stress-modified critical strain and Bao-Wierzbicki ductile damage models for simulating the post-ultimate stress-strain behaviour of shear studs, including fracture, were evaluated. Two calibration methods for the stud tensile and shear damage parameters, based on the Bao-Wierzbicki model, were presented: the first based on stud tensile and shear test data, and the second on stud tensile and push-out test data. The latter method was found to better capture stud behaviour in pushout tests, as it more accurately represented the stress state in the push-out specimens, and was therefore recommended.

Furthermore, the review of the literature highlighted a lack of consensus on the correct approaches for modelling boundary conditions, and for the appropriate values of friction coefficient in contact definitions. The proposed modelling framework includes a new approach for modelling the boundary conditions at the base of the slab which more accurately represents the experimental conditions when the slabs are

embedded in grout or plaster. Sensitivity studies have been carried out on contact friction coefficients and CDP viscosity parameters.

The proposed modelling framework was validated against several experimental tests from the literature [4,16,28], demonstrating its capability to capture a wide range of geometric and material properties in push-out tests, including carbon steel, austenitic stainless steel and duplex stainless steel studs with varying diameters. This approach comprehensively accounted for all relevant modelling parameters influencing the structural behaviour of push-out specimens. It achieved higher predictive accuracy in the overall load-slip response compared to existing methods and successfully replicated the observed failure modes. The proposed modelling framework can be used to capture the behaviour of a variety of push-out arrangements with welded headed shear studs, with different concrete grades, stud grades, stud heights, stud diameters and stud arrangements. This is ideal for the development of extensive parametric analyses of stainless steel pushout tests, which would aid in the assessment of Eurocode 4 design equations for predicting the resistance of welded stainless steel shear studs in composite beams.

CRediT authorship contribution statement

R. Presswood: Writing – original draft, Methodology, Validation, Formal analysis. M. Shaheen: Supervision, Writing – review & editing, Conceptualization. S. Afshan: Writing – review & editing, Conceptualization, Supervision. F. Meza: Writing – review & editing. N. Baddoo: Writing – review & editing.

Declaration of competing interest

The authors declare that they have no known competing financial interests or personal relationships that could have appeared to influence the work reported in this paper.

Acknowledgments

The authors gratefully acknowledge the University of Southampton PhD studentship funding, which enabled this project to be carried out.

Data availability

Data will be made available on request.

References

- BSI, Eurocode 4: Design of composite steel and concrete structures Part 1-1: General rules and rules for buildings, British Standards Institution, 2004.
- [2] R.P. Johnson, D.J. Oehlers, Analysis and design for longitudinal shear in composite T-beams, Proc. Inst. Civ. Eng. 71 (1981) 989–1021, http://dx.doi. org/10.1680/iicep.1981.1735.
- [3] S. Hicks, Longitudinal Shear Resistance of Steel and Concrete Composite Beams (Ph.D. thesis), University of Cambridge, 1997.
- [4] S.W. Pathirana, B. Uy, O. Mirza, X. Zhu, Bolted and welded connectors for the rehabilitation of composite beams, J. Constr. Steel Res. 125 (2016) 61–73, http://dx.doi.org/10.1016/j.jcsr.2016.06.003.
- [5] C. Xu, Q. Su, H. Masuya, Static and fatigue behavior of the stud shear connector in lightweight concrete, Int. J. Steel Struct. 18 (2018) 569–581, http://dx.doi. org/10.1007/s13296-018-0014-1.
- [6] D. Kruszewski, A. Zaghi, K. Wille, Finite element study of headed shear studs embedded in ultra-high performance concrete, Eng. Struct. 188 (2019) 538–552, http://dx.doi.org/10.1016/j.engstruct.2019.03.035.
- [7] U. Katwal, Z. Tao, M.K. Hassan, B. Uy, D. Lam, Load sharing mechanism between shear studs and profiled steel sheeting in push tests, J. Constr. Steel Res. 174 (2020) http://dx.doi.org/10.1016/j.jcsr.2020.106279.
- [8] Y. Li, S. Wang, G. Zhao, Y. Ma, D. Guo, J. Luo, Z. Fang, E. Fang, Shear behavior of short studs in steel-thin ultrahigh-performance concrete composite structures, Case Stud. Constr. Mater. 19 (2023) http://dx.doi.org/10.1016/j.cscm. 2023.e02423.
- [9] Y. Zhou, B. Uy, J. Wang, D. Li, X. Liu, Behaviour and design of stainless steel shear connectors in composite beams, Steel Compos. Struct. 46 (2023) 175–193, http://dx.doi.org/10.12989/scs.2023.46.2.175.

- [10] D. Lam, E. Ellobody, Behavior of headed stud shear connectors in composite beam, J. Struct. Eng. 131 (2005) 96–107, http://dx.doi.org/10.1061/(ASCE) 0733-9445(2005)131:1(96).
- [11] M. Pavlović, Z. Marković, M. Veljković, D.B.D. Signevac, Bolted shear connectors vs. headed studs behaviour in push-out tests, J. Constr. Steel Res. 88 (2013) 134–149, http://dx.doi.org/10.1016/j.jcsr.2013.05.003.
- [12] E. Tzouka, T. Karavasilis, M. Kashani, S. Afshan, Finite element modelling of push-out tests for novel locking nut shear connectors, Structures 33 (2021) 1020–1032, http://dx.doi.org/10.1016/j.istruc.2021.04.088.
- [13] J. He, A. Suwaed, G. Vasdravellis, Horizontal pushout tests and parametric analyses of a locking-bolt demountable shear connector, Structures 35 (2022) 667–683, http://dx.doi.org/10.1016/j.istruc.2021.11.041.
- [14] E. Schedin, A. Backhouse, Stainless Steel Composite Bridge Study A Summary of ARUP Reports, Tech. Rep., Outokumpu, 2019.
- [15] F. Meza, N. Baddoo, Life Cycle Cost Assessment of a Stainless Steel Highway Bridge, The Steel Construction Institute, 2023.
- [16] R. Presswood, S. Afshan, F. Meza, N. Baddoo, M. Shaheen, P. Desnerck, Experimental study on the behaviour of austenitic stainless steel and carbon steel welded shear connectors, Eng. Struct. 321 (2024) http://dx.doi.org/10.1016/j. engstruct.2024.118930.
- [17] Dassault, ABAQUS Analysis User's Manual 6.10-EF, Providence, RI, USA, 2010.
- [18] Y. Song, J. Wang, B. Uy, D. Li, Experimental behaviour and fracture prediction of austenitic stainless steel bolts under combined tension and shear, J. Constr. Steel Res. 166 (2020) 105916, http://dx.doi.org/10.1016/j.jcsr.2019.105916.
- [19] Y. Bao, T. Wierzbicki, On fracture locus in the equivalent strain and stress triaxiality space, Int. J. Mech. Sci. 46 (2004) 81–98, http://dx.doi.org/10.1016/ j.ijmecsci.2004.02.006.
- [20] L. An, K. Cederwall, Push-out tests on studs in high strength and normal strength concrete, J. Constr. Steel Res. 36 (1996) 15–29.
- [21] M. Spremic, Z. Markovic, M. Veljkovic, D. Budjevac, Push-out experiments of headed shear studs in group arrangements, Adv. Steel Constr. 9 (2013) 139–160.
- [22] M. Qasem, M. Hasan, R. Muhamad, C.L. Chin, N. Alanazi, Generalised calibration and optimization of concrete damage plasticity model for finite element simulation of cracked reinforced concrete structures, Results Eng. 25 (2025) http://dx.doi.org/10.1016/j.rineng.2024.103905.
- [23] D. Carreira, K.-H. Chu, Stress-strain relationship for plain concrete in compression, ACI J. (1985).
- [24] F. Mcclintock, Local criteria for ductile fracture, Int. J. Fract. Mech. 4 (1968).
- 25] J. Rice, D. Tracey, On the ductile enlargements of voids in triaxial stress fields, J. Mech. Phys. Solids 17 (1969).
- [26] Y. Ling, Uniaxial true stress-strain after necking, AMP J. Technol. 5 (1996).
- [27] I.R. Gomez, Behavior and Design of Column Base Connections (Ph.D. thesis), University of California, 2010.
- [28] Y. Zhou, B. Uy, X. Liu, D. Li, Finite element modelling of stainless steel shear connectors in composite beams, in: Advances in Structural Engineering and Mechanics ASEM19, 2019, pp. 1–14.
- [29] FIB, CEB FIP Model Code 2010, Tech. Rep., FIB, 2010.